



Bi-directional tuning of thermal transport in SrCoO_x with electrochemically induced phase transitions

Qiyang Lu^{1,2,6}, Samuel Huberman^{3,6}, Hantao Zhang^{1,4}, Qichen Song³, Jiayue Wang^{1,4}, Gulin Vardar^{1,4}, Adrian Hunt⁵, Iradwikanari Waluyo⁵, Gang Chen³ and Bilge Yildiz^{1,2,4}

Unlike the wide-ranging dynamic control of electrical conductivity, there does not exist an analogous ability to tune thermal conductivity by means of electric potential. The traditional picture assumes that atoms inserted into a material's lattice act purely as a source of scattering for thermal carriers, which can only reduce thermal conductivity. In contrast, here we show that the electrochemical control of oxygen and proton concentration in an oxide provides a new ability to bi-directionally control thermal conductivity. On electrochemically oxygenating the brownmillerite $\text{SrCoO}_{2.5}$ to the perovskite $\text{SrCoO}_{3-\delta}$, the thermal conductivity increases by a factor of 2.5, whereas protonating it to form hydrogenated $\text{SrCoO}_{2.5}$ effectively reduces the thermal conductivity by a factor of four. This bi-directional tuning of thermal conductivity across a nearly 10 ± 4 -fold range at room temperature is achieved by using ionic liquid gating to trigger the 'tri-state' phase transitions in a single device. We elucidated the effects of these anionic and cationic species, and the resultant changes in lattice constants and lattice symmetry on thermal conductivity by combining chemical and structural information from X-ray absorption spectroscopy with thermoreflectance thermal conductivity measurements and ab initio calculations. This ability to control multiple ion types, multiple phase transitions and electronic conductivity that spans metallic through to insulating behaviour in oxides by electrical means provides a new framework for tuning thermal transport over a wide range.

An ability to tune thermal conductivity on demand over a wide range by means of applied electrical bias is desirable¹. Such a capability could enable novel applications by use of an 'electrical heat valve'; that is, the application of a voltage difference tunes the extent of heat flow by changing the material intrinsic properties on demand. There are a few processes that could be manipulated by electric potential and ultimately affect thermal transport in a given material, which include, but are not limited to, the atomic or defect composition and the atomic structure. Insertion of atoms into the lattices of materials usually leads to defects that reduce the thermal conductivity due to an increased phonon scattering². For example, the impact of Li^+ ion intercalation on thermal conductivity has been theoretically investigated in graphite³ and experimentally assessed in MoS_2 (ref. 4). Both studies report a decrease of thermal conductivity with increasing Li^+ ion concentration, down to one-fifth of the original value. A comparable reduction in thermal conductivity was found by the intercalation of Li^+ in black phosphorus⁵. Defects are not guaranteed to yield large effects in all materials; for instance, only a negligible effect of oxygen non-stoichiometry on thermal conductivity was reported for $\text{La}_{0.5}\text{Sr}_{0.5}\text{CoO}_3$ thin films⁶. More recently, the static insertion and removal of ions was extended to a dynamic process via Li^+ ion intercalation in the LiCoO_2 electrodes of electrochemical cells, which yielded reversible changes of ~1.5- to 2.7-fold in thermal conductivity⁷. Beyond the insertion and removal of ions, the second strategy for dynamically controlling thermal conductivity involves the modification of the crystal structure and lattice parameters, and the concomitant properties of thermal carriers (that is, phonon dispersion, modewise specific heats, group velocities and lifetimes) via the application of mechanical,

thermal or electrical work. For instance, molecular dynamics simulations show a moderate dependence of thermal conductivity on strain for silicon^{8,9}. Examples of temperature-induced phase transitions include the metal-to-insulator transition in VO_2 that occurs at ~340 K to affect the thermal conductivity by ~30% (ref. 10). Similarly, in PbTiO_3 thin films, a ~15% change in thermal conductivity due to changes in the ferroelectric domain density as a function of electric field was reported¹¹. However, thus far a wide-ranging on-demand modulation of thermal conductivity by the electrical control of either ions or crystal structure remains missing.

In this work, we make use of the interplay between ionic defects and atomic structure—ions are electrochemically inserted into strontium cobalt oxide ($\text{SrCoO}_{2.5}$ (SCO)) thin films and trigger phase transitions to yield large changes in thermal conductivity at room temperature. This large tuning range is achieved by spanning three distinct phases induced via the incorporation of two different ions, H^+ and O^{2-} . We chose SCO as the material system of interest due to the 'tri-state' phase transitions achieved by incorporating ionic species on ionic liquid gating¹². Therefore, in this system the phase transitions are essentially controlled by the amount of oxide ions and protons in SCO. More specifically, the phase transition from the Brownmillerite phase $\text{SrCoO}_{2.5}$ (BM-SCO) to the perovskite phase $\text{SrCoO}_{3-\delta}$ (P-SCO; δ represents oxygen non-stoichiometry) is triggered by applying an anodic bias to oxygenate the SCO^{13,14}. Hydrogenating SCO to form the proton (H^+)-containing H- $\text{SrCoO}_{2.5}$ (H-SCO) is achieved by reversing the polarity of the gating voltages to a cathodic bias. Although the BM-SCO \rightarrow P-SCO phase transition is accompanied by an insulator-to-metal transition^{12,15,16}, the BM-SCO \rightarrow H-SCO transition introduces a further

¹Laboratory for Electrochemical Interfaces, Massachusetts Institute of Technology, Cambridge, MA, USA. ²Department of Materials Science and Engineering, Massachusetts Institute of Technology, Cambridge, MA, USA. ³Department of Mechanical Science and Engineering, Massachusetts Institute of Technology, Cambridge, MA, USA. ⁴Department of Nuclear Science and Engineering, Massachusetts Institute of Technology, Cambridge, MA, USA. ⁵National Synchrotron Light Source II, Brookhaven National Laboratory, Upton, NY, USA. ⁶These authors contributed equally: Qiyang Lu, Samuel Huberman. ✉e-mail: gchen2@mit.edu; byildiz@mit.edu

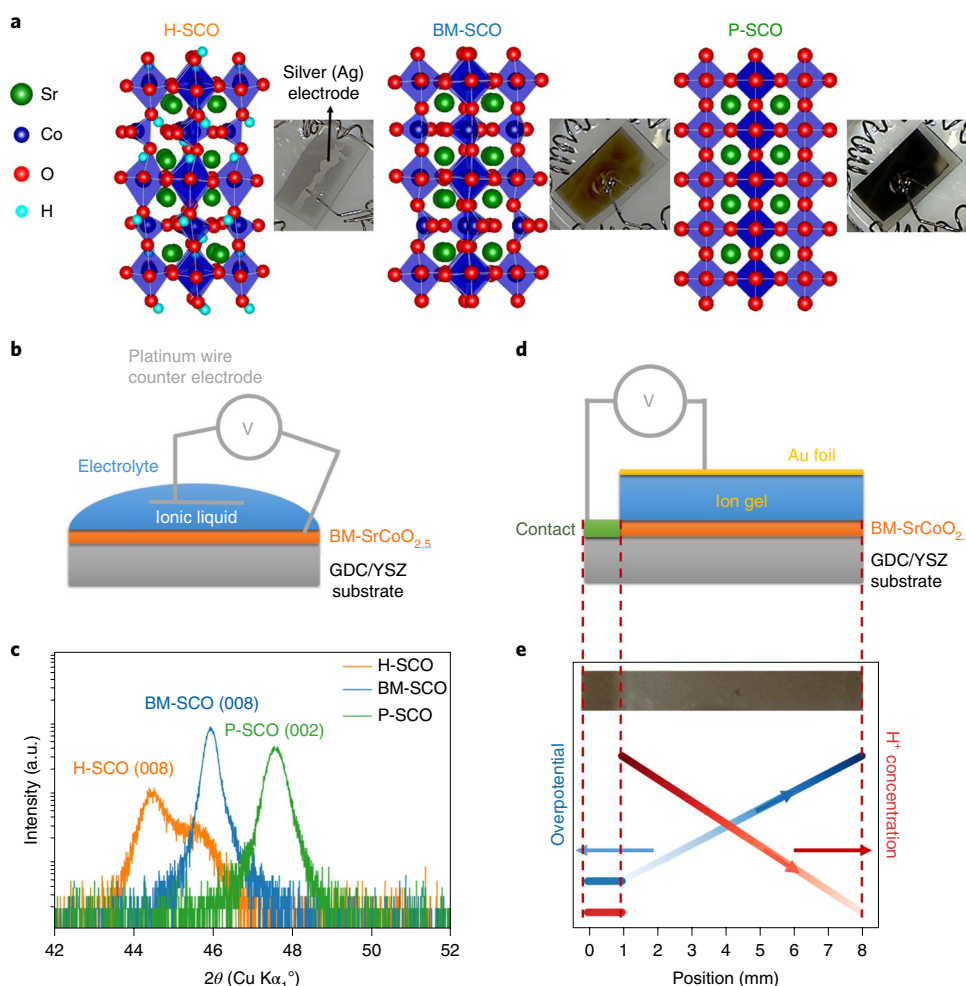


Fig. 1 | Ionic liquid and ion gel gating on the BM-SCO. a, Crystal structure of H-SCO, BM-SCO and P-SCO. Optical pictures of H-SCO, BM-SCO and P-SCO are shown next to the crystal structures of each phase. **b**, Schematic showing the ionic liquid gating of SCO. No metal electrode was deposited on the SCO thin film for the BM-SCO → P-SCO transition. A silver electrode was painted on the top middle of the thin film for enabling the BM-SCO → H-SCO phase transition uniformly (as shown in **a**; see Supplementary Fig. 14 for more details), because of the low electrical conductivity of the H-SCO phase. **c**, XRD showing the BM-SCO(008) diffraction peak, H-SCO (008) peak after -4 V and the P-SCO peak after $+3$ V ionic liquid gating. The shoulder peak in H-SCO at a higher 2θ position is due to the non-switched BM-SCO regions of the sample under the silver electrode used. **d**, Schematic showing the ion gel gating of SCO. **e**, Schematic showing the overpotential distribution in a BM-SCO thin-film sample before the hydrogenation reaction as well as the resulting proton concentration gradient. The overpotential increases with increasing distance away from the contact due to the ohmic loss from the resistance of the SCO thin film, and the potential goes from -4 V to -0 V in this experiment. The dashed lines match the positions in the overpotential gradient with the positions in the optical picture of the sample (inset). Hydrogenation caused a colour change of SCO from brownish (BM-SCO) to light greyish (H-SCO), as seen in the optical picture. a.u., arbitrary units.

opening of the bandgap in SCO¹². The structures of these three phases are shown in Fig. 1a. Given the distinct chemical compositions, crystal and electronic structures of these three phases, it is reasonable to expect a significant change in thermal transport. We hypothesized that the P-SCO phase will have the largest thermal conductivity, as it belongs to the space group with the highest symmetry of the three different phases. It is understood that this relatively increased symmetry consequently imposes a greater number of constraints on the scattering phase space of phonons¹⁷. In addition, P-SCO is a metallic conductor that could contribute to an increased thermal conductivity, although in this case we show later that this is a minor contribution compared to the effects of lattice symmetry, lattice parameter and oxygen defects. However, the phase transition from BM-SCO to H-SCO is expected to decrease the thermal conductivity, due to the creation of more scattering sites introduced by the intercalated protons and larger size of reduced

Co cations. Time-domain thermoreflectance (TDTR) measurements showed that across the BM-SCO → P-SCO phase transition, the thermal conductivity k increased monotonically by a factor of 2.5. This contrasts with the traditional understanding in which the inserted extra atoms only contribute to a reduced thermal conductivity. However, the BM-SCO → H-SCO phase transition decreased k to $\sim 25\%$ of its original value. Combining these bidirectional phase transitions triggered in the same device, we achieved a tunable range of more than one order of magnitude (10 ± 4 -fold change) in thermal conductivity. We also constructed a solid-state version using ion gels capable of producing a fourfold change in thermal conductivity. More importantly, the use of ion gels introduced a lateral gradient of H⁺ concentration in SCO thin films, which allowed us to relate systematically the ionic defect concentration to thermal transport.

Overall, our work provides a new route for tuning thermal conductivity over a wide range by the electrochemical control of

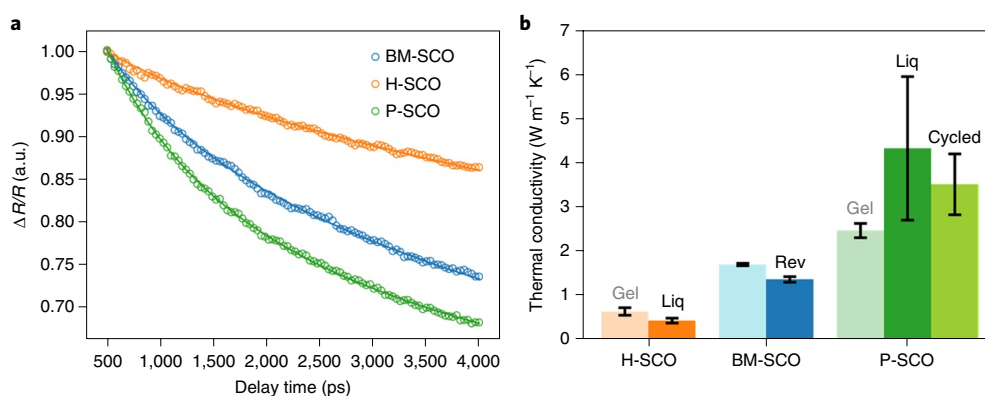
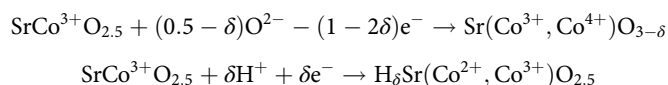


Fig. 2 | Thermal conductivity tuning in SrCoO_x characterized by TDTR measurements. **a**, Raw TDTR data (circles) and best fits (lines) for H-SCO, BM-SCO and P-SCO. The H-SCO and P-SCO were obtained by gating BM-SCO through an ionic liquid. **b**, Thermal conductivity of H-SCO, BM-SCO and P-SCO. H-SCO and P-SCO were obtained by gating either ionic liquid (liq) or ion gel (gel). TDTR measurements were performed on samples with a thin Al transducer layer deposited on top, after cleaning the residue from the ionic liquid or ion gel gating. The thermal conductivities of a BM-SCO thin film subjected to a BM → P → BM cycle and of a P-SCO thin film subjected to BM → P → BM → P cycles, are also shown (marked as 'rev' and 'cycled', respectively); gating was performed by using ionic liquid, and measured only at the final BM-SCO or the final P-SCO state. The error bars are from the variations between several measurement positions laterally on the films. The large error bars for the ionic liquid P-SCO are attributed to the reduction in sensitivity to thermal conductivity compared to the that of the lower thermal conductivity samples (Supplementary Fig. 13).

multiple defect or ion types, atomic structures and electronic structure simultaneously. This approach is substantially different from that using only one ion type and only in one structural phase, which limits the range of thermal conductivity that can be spanned. The here obtained tenfold (10 ± 4) change in thermal conductivity is much larger than previously obtained tunable ranges of thermal conductivity. The use of multiple ions (both oxygens and protons) and multiple phase transitions in a single device is the key to this ability.

Electrochemically induced phase transitions and thermal conductivity modulation in SrCoO_x

Phase transitions in SCO were achieved by intercalating oxygen anions or protons into BM-SCO by using ionic liquid gating with the BM-SCO film as a working electrode, as shown in Fig. 1b. We switched BM-SCO to the oxygenated P-SCO by applying a +3 V gate voltage, and to the hydrogenated phase H-SCO by applying a −4 V gate voltage. The application of gate voltage, or electrical bias, is used as the electrochemical potential that modulate the chemical potential of the oxygen and hydrogen species in the SCO thin films. The oxygenation and hydrogenation electrochemical reactions are shown below. Note here that O^{2−} only represents the formal charge of an ionic species, but not necessarily in the form of 2[−] charged oxide ions:



We confirmed the phase transition by performing X-ray diffraction (XRD) on the switched thin films, as shown in Fig. 1c. The liquid form of the ionic electrolyte allows for a low overpotential and a large driving force for ion intercalation, but the liquid form also imposes constraints in practical device applications. Therefore, we also implemented ion gels for triggering the ion intercalation and phase transition, which is a promising approach for a solid-state application of this concept. The ion gels were fabricated by containing the ionic liquid electrolyte in a block copolymer framework¹⁸. Figure 1d shows a schematic of using ion gels for gating. The oxygenation using ion gels resulted in chemical and structural changes that are similar to those obtained by using ionic liquid gating. A lower oxygen stoichiometry in P-SCO was reached (Supplementary Fig. 1) than achievable by ionic liquid gating. Hydrogenation using

ion gels allowed us to obtain a lateral gradient of H⁺ concentration in the sample (Fig. 1e). Both BM-SCO and H-SCO have a low electrical conductivity, with that of H-SCO being the lowest¹². When we applied electrical bias between the edge of the sample and the top of the ion gel, the hydrogenation reaction was self-limiting due to the difficulty of current collection with high ohmic losses after forming the insulating H-SCO phase. Figure 1e shows schematically the overpotential distribution from the contact to the other end of the BM-SCO sample, before any H-SCO is formed. As shown in Fig. 1e, the electrochemical driving force decreased gradually, starting from the contact region, due to the increased ohmic loss from the resistance of the BM-SCO thin film. The end result was a concentration gradient of H⁺ from the contact area to the other edge of the thin-film sample. As the hydrogenation induced a colour change of SCO, a colour gradient was clearly observed in the optical picture of the sample (Fig. 1e). This concentration gradient provided us with a way to correlate the local H⁺ concentration to the local thermal conductivity, presented later in the paper.

We performed time-domain thermoreflectance (TDTR) measurements on BM-SCO, H-SCO and P-SCO to probe the effect of incorporated ionic species and phase transitions on the thermal transport property^{19–21}. We also performed ab initio calculations to assess the accumulated thermal conductivity as a function of phonon mean free path for P-SCO (Supplementary Fig. 10). We found that when the mean free path reached the thin-film thickness (~40 nm), the accumulated thermal conductivity reached ~93%, which means that the TDTR measurement results can reflect the actual *k* of SCO. Example raw TDTR data are shown in Fig. 2a and the results of fitting are reported in Fig. 2b. We achieved a large range of thermal conductivity modulation by ionic liquid and ion gel gating. The measured thermal conductivity *k* for the as-grown BM-SCO was $1.70 \pm 0.03 \text{ W m}^{-1} \text{ K}^{-1}$. By using ionic liquid gating, we were able to more than double the thermal conductivity on oxygenating SCO to the perovskite phase, to reach a thermal conductivity of $4.33 \pm 1.62 \text{ W m}^{-1} \text{ K}^{-1}$ for P-SCO. This thermal conductivity value was averaged from four different samples (Supplementary Fig. 16), and multiple spots were measured on each sample to represent the sample-to-sample and within-sample variability. The variability among the measured values can arise from different amounts and types of defects, which include oxygen vacancies and extended defects such as dislocations in the SCO films. The measured

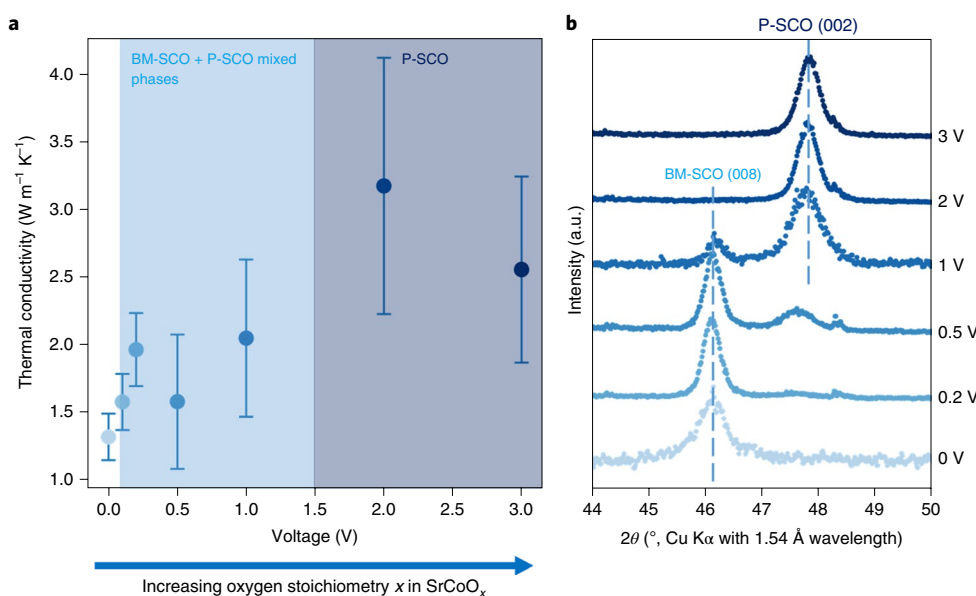


Fig. 3 | Effect of oxygen stoichiometry (x) on the thermal conductivity of SrCoO_x . **a**, Thermal conductivity of SrCoO_x , measured at room temperature on samples quenched from 300 °C, as a function of applied electrical bias (anodic) by using YSZ as a solid gating electrolyte at 300 °C. Note that the oxygen stoichiometry x in SrCoO_x increases monotonically as a function of the applied electrical bias, as indicated by the arrow below the voltage axis. **b**, XRD results for SrCoO_x on applying the electrochemical potentials shown in **a**. At 0 V, the phase is pure BM. The gradual transition from a mixture of BM-SCO and P-SCO phases to a single P-SCO phase was observed with increasing voltage, as indicated by the shaded voltage regimes in **a**.

electrical resistivity of the P-SCO phase is $5 \times 10^{-2} \Omega \text{cm}$ (Methods). Using this value and the Weidemann–Franz law, one expects a thermal conductivity of $\sim 0.07 \text{ W m}^{-1} \text{ K}^{-1}$, significantly lower than the measured $4.33 \pm 1.62 \text{ W m}^{-1} \text{ K}^{-1}$. This suggests that phonons, and not electrons, are the dominant thermal carriers in the P-SCO phase. Our measured value of k for P-SCO is comparable with those of other semiconducting oxide perovskite systems²². In addition, by hydrogenating the BM-SCO to obtain H-SCO, the thermal conductivity was lowered to $0.44 \pm 0.06 \text{ W m}^{-1} \text{ K}^{-1}$, which is less than about a fourth of the k of BM-SCO. This bi-directional tuning of thermal conductivity by simply reversing the polarity and using multiple ion insertions is a novel phenomenon not reported in previous literature. The combined 9.8 ± 3.9 -fold (rounded to 10 ± 4) change in thermal conductivity surpasses other reports in the literature on tuning thermal transport using ionic species^{6,7,23}. We also measured the thermal conductivity of the three SCO phases as a function of temperature (Supplementary Fig. 13). The tunable range of thermal conductivity increases at lower temperatures.

Tunable thermal conductivity can also be obtained by ion gel (semi-solid) gating, albeit the tunable range was smaller compared with that of ionic liquid gating, probably due to the different potential distribution achieved using the ionic gel compared to that using the ionic liquid electrolyte. The measured thermal conductivities k for P-SCO and H-SCO obtained by gating through ion gels were 2.47 ± 0.16 and $0.64 \pm 0.09 \text{ W m}^{-1} \text{ K}^{-1}$, respectively (this value of $k_{\text{H-SCO}}$ was measured at the regions of highest hydrogenation). The lower thermal conductivity of P-SCO (gel) is very likely linked to a lower oxygen stoichiometry (Supplementary Fig. 1), as we found a correlation between oxygen vacancy concentration and measured k in P-SCO (Supplementary Fig. 17).

In theory, the concept of tuning the thermal conductivity by using the BM \rightarrow P phase transition is reversible because it relies on solid-state electrochemistry and defect chemistry (oxygen content in this case) that is altered thermodynamically by applying an electrochemical potential. This is in line with the previous report by Lu et al., which shows that both BM \rightarrow P and BM \rightarrow H-SCO phase transitions can be reversible for multiple cycles¹². Both the structure

and the physical properties (electrical conductivity and magnetism) were comparable between multiple cycles in that work. Therefore, it is reasonable to expect that the obtained thermal conductivity should also be reversible. On switching the sample back to the BM phase from the P-SCO phase by using a reverse gating voltage of -4 V via ionic liquid, the k value reduced to $1.36 \pm 0.06 \text{ W m}^{-1} \text{ K}^{-1}$ ('rev' in Fig. 2b). The slightly lower thermal conductivity compared with that of the as-prepared BM-SCO samples might be due to additional defects or disordering induced by the switching cycle. Moreover, we measured the thermal conductivity of a P-SCO sample after two cycles of gating in ionic liquid, that is BM \rightarrow P \rightarrow BM \rightarrow P. The k value of this P-SCO ('cycled' P-SCO in Fig. 2b) after two cycles was much higher than that of the pristine BM-SCO sample (Supplementary Fig. 15). However, we also observed the partial dissolution of thin films in the liquid electrolyte experiment after two cycles of phase transition. We observed that the film thickness decreased from 44 to 27 nm after two BM \rightarrow P cycles. To improve the cyclability and practicality of thermal conductivity tuning in SCO, further studies are needed to understand the dissolution mechanism of SCO and come up with solutions to avoid it. We believe that the reversibility of the thermal conductivity of SCO thin films can be improved by optimizing the experimental conditions (that is, amplitude and duration of the applied bias, type of ionic liquid, design of the electrochemical cell and possibly a solid-state configuration).

The effect of oxygenation on the thermal conductivity of SCO

First we discuss the increased thermal conductivity induced by the BM \rightarrow P phase transition—the decrease that arises from the BM-SCO \rightarrow H-SCO phase transition is discussed later. As defects (vacancy, interstitial, substitutional and so on) are introduced into a perfect crystal, the thermal conductivity usually decreases because these defects provide additional scattering sites experienced by thermal energy carriers²⁴. In this sense, the increase of thermal conductivity with the electrochemical oxygenation of BM-SCO is surprising. To better understand the mechanism of the increase in thermal conductivity, we measured additional SrCoO_x samples with different oxygen stoichiometry, as shown in Fig. 3a.

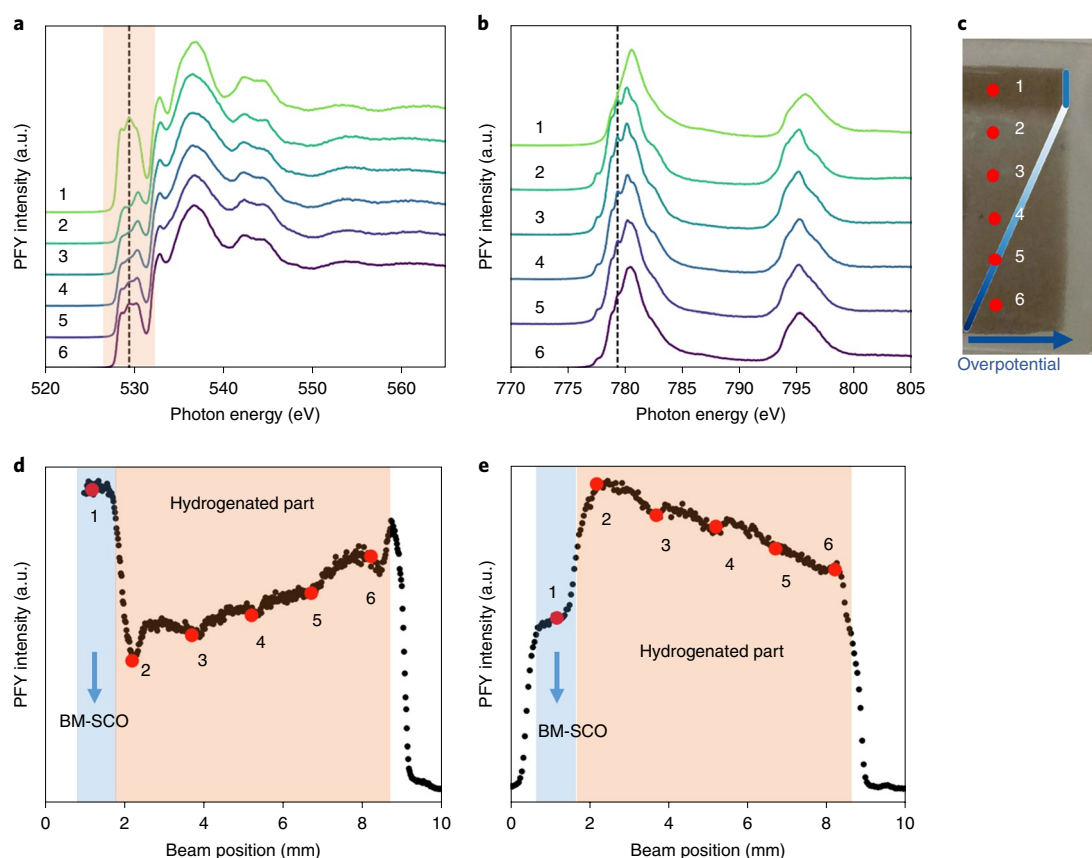


Fig. 4 | X-ray absorption spectra collected using the partial-fluorescence-yield (PFY) mode on the H-SCO thin film by using ion gel. **a, b**, O K-edge (**a**) and Co L-edge (**b**) spectra measured at different positions on the sample. **c**, The measurement positions 1–6, with a sketch of the overpotential distribution in the SCO thin film (Fig. 1d), that is, 1 is the as-grown BM-SCO region, 2 has the highest proton concentration and going from 2 to 6 the concentration of protons decreases. The shaded part in **a** shows the pre-edge peak region in which appreciable changes in the spectrum were observed. The dashed lines in **a** and **b** indicate the photon energies used for the line scans in **d** and **e**. **d, e**, Line scans at a fixed photon energy of 529.4 eV (**d**, in the range of the O K-edge pre-edge peak, indicated by the dashed line in **a**) and 779.4 eV (**e**, in the range of the Co L_3 edge, indicated by the dashed line in **b**). Positions 1–6 shown in red in these two plots correspond to the positions shown on the sample image in **c**.

This stepwise tuning of stoichiometry was achieved by applying electrical biases onto the SCO thin films on yttria-stabilized zirconia (YSZ) substrates at 300 °C. As YSZ conducts oxide ions at elevated temperatures, here we use YSZ as a solid electrolyte through which we electrochemically pump oxygen into BM-SCO, as detailed in our recent work^{13,14}. In principle, this is also possible by using the ionic liquid electrolyte, but it is not yet possible to control the tuning parameters to obtain controllably different oxygen stoichiometries in this experimental geometry. On electrochemical insertion of oxygen into BM-SCO on YSZ at 300 °C, the samples were quenched down to room temperature, and their structure and thermal conductivity were measured. We used seven different samples prepared in the same batch, which were subjected to applied voltages of different magnitudes. Where the mixed phase was obtained electrochemically, our starting point was highly textured BM-SCO thin films grown on YSZ substrates with a gadolinia-doped ceria buffer layer. We estimated the grain size should then be close to the thickness of the thin films (on the order of tens of nanometres). Therefore, as the grain size is sufficiently small, the laser spot size ($\sim 12 \mu\text{m}$) we use should cover a very large number of grains and/or domains. For the phase transition to mixed BM and P phases, we believe that it follows a nucleation–growth process as shown in our previous study¹³. As the nucleation process is random, the formed perovskite grain size should also be similar to the grain size of the starting BM-SCO thin films. Therefore, TDTR measurements should be representative

of the thermal conductivity averaging BM and P domains. We also measured at different spots of the sample to make sure that the reported values approached the average of the whole thin film. We found that applying moderate electrical biases (≤ 1 V) induced a partial phase transition, as shown by the XRD patterns in Fig. 3b. At 2 V and above, the transition from BM-SCO to P-SCO was complete. This finding is consistent with literature reports that reaching a certain oxygen stoichiometry ($x \approx 2.75$, as in SrCoO_x) in SCO is needed to complete the BM \rightarrow P phase transition^{13,14,25,26}. The mixtures of BM-SCO and P-SCO (< 2 V in Fig. 3a) had higher thermal conductivities than that of the as-prepared pure BM-SCO at 0 V, presumably because the P-SCO phase has a higher thermal conductivity. This is probably due, in part, to its higher symmetry compared to that of the BM-SCO phase. To probe the symmetry effect, we calculated the total three-phonon phase space of stoichiometric BM-SCO and stoichiometric P-SCO. We found that the phase space of BM-SCO is nearly two orders of magnitude larger than that of P-SCO. Such a large phase-space difference due to different extents of symmetry plays an important role in causing a large thermal conductivity difference between BM-SCO and P-SCO (see Supplementary Section 10 for more details). On the completion of the BM \rightarrow P phase transition, k continues to increase with increasing oxygenation, which indicates that the oxygen vacancies in P-SCO now assume the role of the ‘traditional’ defect (more details in Supplementary Figs. 1 and 17). In other words, the P-SCO phase is now the perfect crystal in which the vacancies

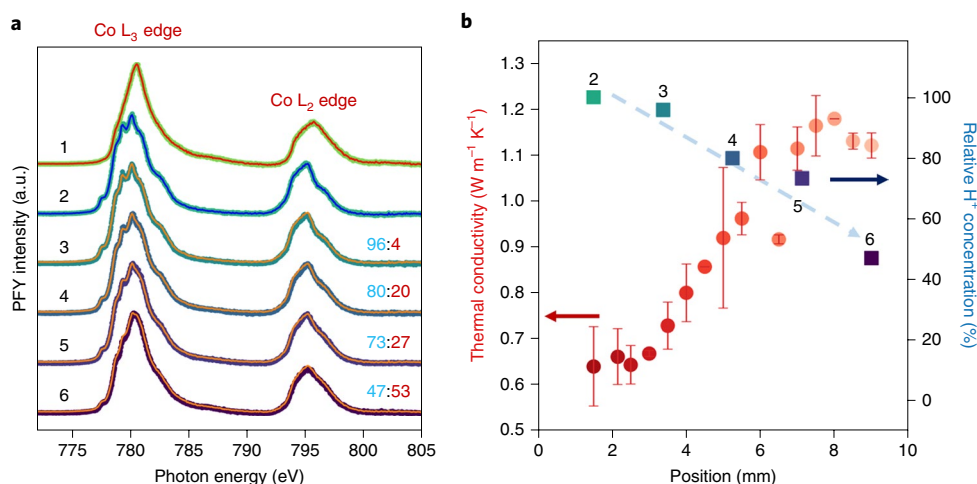


Fig. 5 | The effect of H^+ concentration on the thermal transport property of SCO. **a**, Co $L_{2,3}$ -edge XAS spectra fitted with linear combinations of spectra measured at spot 1 and 2, close to the Co^{3+} and Co^{2+} states, respectively. The symbols are measured data and the lines are the fitting. The numbers next to spectra 2–6 indicate the fraction (in %) of spectrum 1 (in blue) and spectrum 2 (in red). **b**, Thermal conductivity (red symbols) of ion gel H-SCO measured along the H^+ concentration gradient. The error bars represent the standard deviations from measurements at different frequencies at each position. In the same plot, the relative H^+ concentrations deduced from the spectra fitting results in **a** are plotted as square symbols, referenced to the spectrum measured at spot 2. The dashed arrow is only a guide to the eye, showing the direction from spot 2 to spot 6. The positions of the measurement spots 1–6 are shown Fig. 4c.

act as a scattering source for phonons. This is also consistent with our theoretical calculations on the effect of oxygen vacancies on k (Supplementary Fig. 11), which showed an increasing thermal conductivity with decreasing amounts of oxygen vacancies.

Another factor that can contribute to the thermal conductivity increase is the change in lattice parameter on the BM \rightarrow P phase transition due to the change in oxygen stoichiometry in a given phase (the so-called chemical expansion/contraction²⁷). It is known that both the BM \rightarrow P phase transition and the increase in oxygen stoichiometry in P-SCO (x in $SrCoO_x$) contract the lattice. To capture the possible effect of the lattice parameter, we performed ab initio computations on P-SCO in which the change in lattice parameter is manifested as isotropic strain (Supplementary Fig. 12). We found that an isotropic tensile strain (lattice expansion) led to a decreased thermal conductivity, consistent with that predicted for Si (ref. 8) and the experimental results shown for WO_3 in the literature²⁸. Furthermore, the effect of strain (shown in Supplementary Fig. 12) is nearly linear with the change in lattice parameter (bond length). Given that the lattice contracts on going from BM-SCO to P-SCO, the observed increase in thermal conductivity is consistent with the predicted increase in thermal conductivity on lattice contraction. Thus, the change in the lattice constant or bond lengths that affect the phonon scattering behaviour may explain the increased thermal conductivity we observed on the BM \rightarrow P-SCO transition. Nevertheless, we have to recall that the changes in lattice constant and oxygen stoichiometry are correlated in $SrCoO_x$, as well as in other transition metal oxides²⁷. The stated simulations shown in Supplementary Fig. 12 took into consideration only the lattice constant, but not the equilibrium concentration of oxygen defects at that lattice constant. Therefore, the present simulations cannot quantitatively capture the decoupling of the strain and point defects, as these two are coupled inherently. When we refer to the ‘effect of oxygen stoichiometry’ in this study, we mean both the effect of point defects as well as a change in the lattice parameter and/or strain. However, it is important to note that both the effect of oxygen vacancies (Supplementary Fig. 11) and the effect of the lattice parameter (Supplementary Fig. 12) point in the same direction; that is, in going from BM- to P-SCO, the lattice contracts and oxygen vacancies decrease, and both of these are predicted to increase

the thermal conductivity. Therefore, we conclude that the increased thermal conductivity in P-SCO is governed by a combination of changes in the lattice symmetry, lattice constant and oxygen defect concentration.

The effect of hydrogenation on the thermal conductivity of SCO

As shown in the optical photograph in Fig. 1e, we induced a proton concentration gradient laterally along the SCO sample by using ion gel gating. This provided us with a novel experimental scheme to correlate the effect of the ion defect (proton) concentration to the thermal transport property. Soft X-ray absorption spectroscopy (XAS) on this sample revealed the chemical states of the material at different stages of hydrogenation. The beam size of the synchrotron X-rays used was roughly $200 \mu m \times 100 \mu m$, and therefore we could obtain sufficient spatial resolution for the chemical state of SCO at different H^+ concentrations. Figure 4a,b summarizes the XAS data obtained at different spots of the H-SCO, as well as line scan across the H^+ concentration gradient (Fig. 4d,e). O K edge and Co $L_{2,3}$ edge spectra are shown in Fig. 4a,b, respectively. Position 1 in Fig. 4c was the as-grown SCO used as the contact (Fig. 1d). The concentration of H^+ decreases following the direction from position 2 to position 6 (Fig. 1e). As a result, we observed an increase of the pre-edge peak (~ 529 eV) intensity from position 2 to position 6 in the O K-edge spectra. As the pre-edge peak represents the number of ligand holes in O $2p$ orbitals^{14,29,30}, a lower intensity of the pre-edge peak indicates a more reduced chemical state and therefore a higher H^+ concentration. The pre-edge peak intensity at position 6 is lower than that in the spectra at position 1 (BM-SCO), which indicates this position also has some hydrogen concentration. The same trend was observed also in the Co $L_{2,3}$ edge (Fig. 4b). The spectrum at position 1 matches the spectrum reported in the literature for the Co^{3+} oxidation state in BM-SCO³¹. The spectrum at position 2 is similar to that of Co^{2+} with multiple splitting observed in the Co L_3 -edge region, as in H-SCO³². This is again an indication of H^+ incorporation. The spectra measured at positions 3–6 can be treated as a linear combination of the spectra at 1 and 2, that is, a mixed Co^{3+}/Co^{2+} oxidation state, which is discussed in detail later.

To confirm the gradual change in the H^+ concentration laterally on the H-SCO sample, we performed line scans at fixed photon energies in which the largest changes of intensity occurred in the O K-edge and Co L-edge spectra. Figure 4d,e shows the line scans at photon energies $h\nu$ of 529.4 and 779.4 eV. These photon energies are located at the O K-edge pre-edge peak and the Co L_{3-2} -edge peak, respectively. As shown in the dashed lines in Fig. 4a,b, the intensity at these two energies varied appreciably from positions 2 to 6. As a result, in Fig. 4d,e a linear variation of intensity at the selected photon energies can be seen. This proves that the sample holds a lateral concentration gradient of protons.

We calculated the relative H^+ concentration at different positions of the sample and correlated that to the locally measured thermal conductivity. As mentioned above, the Co L_{3-2} -edge spectra at positions 3–6 showed a mixed Co^{3+}/Co^{2+} oxidation state, and could be fitted by using a linear combination of spectra measured at positions 1 (Co^{3+}) and 2 (close to Co^{2+}). The obtained fitting results shown in Fig. 5a are satisfactory. Using the oxidation state of Co as the direct correlation to H^+ in H-SCO, we plotted the H^+ concentration (Fig. 5b). We scaled the H^+ concentration relative to that at position 2 (where a maximum hydrogenation was achieved). Note that the relative concentration does not represent the actual H^+ concentration, as full hydrogenation might not be actually reached at position 2. As shown by the O K-edge spectra in Fig. 4a, the pre-edge peak was still present at the most hydrogenated position. This indicates that the H^+ concentration introduced by the ion gel gating was lower than that introduced by ionic liquid gating. This is similar to having a lower oxygen content in P-SCO when obtained by the ion gel compared to the ionic liquid gating of BM-SCO (Supplementary Fig. 1). This probably arises from a less ideal contact and potential distribution when using the solid ion gel as the gating electrolyte. The thermal conductivity obtained from TDTR measurements and the H^+ concentration estimated from the spectrum fitting are plotted in Fig. 5b. Here the thermal conductivity decreases with increasing the H^+ concentration, in contrast to the role played by oxygen insertion in the BM \rightarrow P-SCO transition. Three effects are probably responsible for this decrease in k . First is the mass disorder as the H^+ ions occupy interstitial sites in the BM framework¹² (Fig. 1a). Second is the displacement of oxygen ions from their equilibrium positions in the BM structure when they bond with protons¹². And third is the ionic size change of Co cations. H^+ insertion into the BM-SCO reduces the Co cations from 3^+ to 2^+ , which is accompanied by an increase of the Co cation radii. The effect of ionic radius was discussed in our previous work on the $Pr_{0.1}Ce_{0.9}O_{2-\delta}$ (ref. 23), in which it is shown that the significantly larger size of Pr^{3+} compared to Pr^{4+} and the accompanying lattice distortions are the dominant reason behind a decrease in thermal conductivity on reducing $Pr_{0.1}Ce_{0.9}O_{2-\delta}$ (increase in δ). Therefore, it is reasonable to expect a similar effect in H-SCO because of the larger Co^{2+} . Importantly, we point out that, if the alloy model that describes thermal conductivity² were applicable here, we would obtain a minimum thermal conductivity as a function of H^+ concentration while transitioning from BM-SCO to H-SCO. However, our data going up to nearly full hydrogenation using the ionic gel and ionic liquid electrolytes do not present a minimum, but rather a continuous decrease in thermal conductivity between BM-SCO and H-SCO. Further analysis and modelling are warranted in future work to pin down the dominant mechanism responsible for the substantial and continuous decrease in thermal conductivity from BM-SCO to H-SCO.

In summary, we demonstrated the bi-directional tuning of thermal conductivity across one order of magnitude in SCO at room temperature. This large tunable range was obtained by accessing the tri-state phases of SCO electrochemically by applying either a positive electrical bias to insert O^{2-} into BM-SCO and obtain the P-SCO phase, or a negative bias to insert H^+ and obtain the H-SCO phase. By performing the electrochemical oxygenation at 300 °C,

we uncovered that thermal conductivity increases with increasing oxygen stoichiometry due to contributions from defect concentration, lattice parameter and lattice symmetry. We also succeeded in constructing a semi-solid state version of this thermal conductivity control by using ion gels to trigger the phase transition in SCO. By using ion gels, we obtained a concentration gradient of H^+ laterally in the SCO thin films. The H^+ concentration gradient allowed us to correlate the thermal conductivity measured by TDTR and the H^+ concentration measured by XAS. Thermal conductivity decreased monotonically with increasing H^+ concentration. This result indicates that the inserted H^+ ions themselves, as well as the consequent chemical and structural changes, act as phonon-scattering sources. As a result, our work provides a new route for tuning thermal conductivity over a wide range by the electrochemical control of multiple defect or ion types, atomic structures and electronic structure simultaneously. The here obtained tunable (within $0.44\sim 4.33\text{ W m}^{-1}\text{ K}^{-1}$), tenfold (10 ± 4) change in thermal conductivity is large; it is even larger at lower temperatures and it is significantly larger than the tunable thermal conductivity ranges reported previously in the literature. The use of multiple ions (both oxygen anions and protons) and multiple phase transitions in a single device is the key to this ability. There are numerous oxides that exhibit both oxygen non-stoichiometry and H^+ intercalation that are tunable electrochemically, for example, WO_3 , MoO_3 , Nb_2O_5 , Ta_2O_5 , VO_2 and V_2O_5 (ref. 33), and such oxides can also be utilized in a similar way as the SCO system here. Our larger range of tuning thermal conductivity in oxides, compared with previous studies in the literature, provides a new pathway of designing such functional oxides for applications in smart windows³⁴, thermal management and energy harvesting²⁴.

Online content

Any methods, additional references, Nature Research reporting summaries, source data, extended data, supplementary information, acknowledgements, peer review information; details of author contributions and competing interests; and statements of data and code availability are available at <https://doi.org/10.1038/s41563-020-0612-0>.

Received: 18 April 2018; Accepted: 10 January 2020;
Published online: 24 February 2020

References

- Wehmeyer, G., Yabuki, T., Monachon, C., Wu, J. & Dames, C. Thermal diodes, regulators, and switches: Physical mechanisms and potential applications. *Appl. Phys. Rev.* **4**, 041304 (2017).
- Abeles, B. Lattice thermal conductivity of disordered semiconductor alloys at high temperatures. *Phys. Rev.* **131**, 1906–1911 (1963).
- Qian, X., Gu, X., Dresselhaus, M. S. & Yang, R. Anisotropic tuning of graphite thermal conductivity by lithium intercalation. *J. Phys. Chem. Lett.* **7**, 4744–4750 (2016).
- Zhu, G. et al. Tuning thermal conductivity in molybdenum disulfide by electrochemical intercalation. *Nat. Commun.* **7**, 13211 (2016).
- Kang, J. S., Ke, M. & Hu, Y. Ionic intercalation in two-dimensional van der Waals materials: in situ characterization and electrochemical control of the anisotropic thermal conductivity of black phosphorus. *Nano Lett.* **17**, 1431–1438 (2017).
- Wu, X. et al. Glass-like through-plane thermal conductivity induced by oxygen vacancies in nanoscale epitaxial $La_{0.5}Sr_{0.5}CoO_{3-\delta}$. *Adv. Funct. Mater.* **27**, 1704233 (2017).
- Cho, J. et al. Electrochemically tunable thermal conductivity of lithium cobalt oxide. *Nat. Commun.* **5**, 1–6 (2014).
- Li, X., Maute, K., Dunn, M. L. & Yang, R. Strain effects on the thermal conductivity of nanostructures. *Phys. Rev. B* **81**, 1–11 (2010).
- Murphy, K. F., Piccione, B., Zanjani, M. B., Lukes, J. R. & Gianola, D. S. Strain- and defect-mediated thermal conductivity in silicon nanowires. *Nano Lett.* **14**, 3785–3792 (2014).
- Kizuka, H. et al. Temperature dependence of thermal conductivity of VO_2 thin films across metal–insulator transition. *Jpn J. Appl. Phys.* **54**, 053201 (2015).

11. Ihlefeld, J. F. et al. Room-temperature voltage tunable phonon thermal conductivity via reconfigurable interfaces in ferroelectric thin films. *Nano Lett.* **15**, 1791–1795 (2015).
12. Lu, N. et al. Electric-field control of tri-state phase transformation with a selective dual-ion switch. *Nature* **546**, 124–128 (2017).
13. Lu, Q., Chen, Y., Bluhm, H. & Yildiz, B. Electronic structure evolution of SrCoO_x during electrochemically driven phase transition Probed by in situ X-ray Spectroscopy. *J. Phys. Chem. C* **120**, 24148–24157 (2016).
14. Lu, Q. & Yildiz, B. Voltage-controlled topotactic phase transition in thin-film SrCoO_x monitored by in situ X-ray diffraction. *Nano Lett.* **16**, 1186–1193 (2016).
15. Jeon, H. et al. Reversible redox reactions in an epitaxially stabilized SrCoO_x oxygen sponge. *Nat. Mater.* **12**, 1057–1063 (2013).
16. Choi, W. S. et al. Reversal of the lattice structure in SrCoO_x epitaxial thin films studied by real-time optical spectroscopy and first-principles calculations. *Phys. Rev. Lett.* **111**, 1–5 (2013).
17. Lindsay, L. & Broido, D. A. Three-phonon phase space and lattice thermal conductivity in semiconductors. *J. Phys. Condens. Matter* **20**, 165209 (2008).
18. Lee, K. H. et al. 'Cut and stick' rubbery ion gels as high capacitance gate dielectrics. *Adv. Mater.* **24**, 4457–4462 (2012).
19. Capinski, W. S. & Maris, H. J. Improved apparatus for picosecond pump-and-probe optical measurements. *Rev. Sci. Instrum.* **67**, 2720–2726 (1996).
20. Cahill, D. G., Goodson, K. & Majumdar, A. Thermometry and thermal transport in micro/nanoscale solid-state devices and structures. *J. Heat. Transf.* **124**, 223 (2002).
21. Schmidt, A. J., Chen, X. & Chen, G. Pulse accumulation, radial heat conduction, and anisotropic thermal conductivity in pump-probe transient thermoreflectance. *Rev. Sci. Instrum.* **79**, 114902 (2008).
22. van Roekeghem, A., Carrete, J., Oses, C., Curtarolo, S. & Mingo, N. High-throughput computation of thermal conductivity of high-temperature solid phases: the case of oxide and fluoride perovskites. *Phys. Rev. X* **6**, 41061 (2016).
23. Luckyanova, M. N. et al. Thermal conductivity control by oxygen defect concentration modification in reducible oxides: the case of Pr_{0.1}Ce_{0.9}O_{2-δ} thin films. *Appl. Phys. Lett.* **104**, 061911 (2014).
24. Toberer, E. S., Baranowski, L. L. & Dames, C. Advances in thermal conductivity. *Annu. Rev. Mater. Res.* **42**, 179–209 (2012).
25. Lee, J. H. et al. Strongly coupled magnetic and electronic transitions in multivalent strontium cobaltites. *Sci. Rep.* **7**, 16066 (2017).
26. Nemudry, a, Rudolf, P. & Schöllhorn, R. Topotactic electrochemical redox reactions of the defect perovskite SrCoO_{2.5+x}. *Chem. Mater.* **4756**, 2232–2238 (1996).
27. Bishop, S. R. et al. Chemical expansion: implications for electrochemical energy storage and conversion devices. *Annu. Rev. Mater. Res.* **44**, 205–239 (2014).
28. Ning, S. et al. Anomalous defect dependence of thermal conductivity in epitaxial WO₃ thin films. *Adv. Mater.* **31**, 1903738 (2019).
29. Hu, Z. et al. Hole distribution between the Ni 3d and O 2p orbitals in Nd_{2-x}Sr_xNiO_{4-δ}. *Phys. Rev. B* **61**, 3739–3744 (2000).
30. Abbate, M. et al. Controlled-valence properties of La_{1-x}Sr_xFeO₃ and La_{1-x}Sr_xMnO₃ studied by soft-X-ray absorption spectroscopy. *Phys. Rev. B* **46**, 4511–4519 (1992).
31. Abbate, M. et al. Electronic structure and spin-state transition of LaCoO₃. *Phys. Rev. B* **47**, 16124–16130 (1993).
32. Burnus, T. et al. Valence, spin, and orbital state of Co ions in one-dimensional Ca₃Co₂O₆: an X-ray absorption and magnetic circular dichroism study. *Phys. Rev. B* **74**, 245111 (2006).
33. Fripiat, J. J. & Lin, X. Hydrogen intercalation within transition metal oxides: entropy, enthalpy, and charge transfer. *J. Phys. Chem.* **96**, 1437–1444 (1992).
34. Cai, G., Wang, J. & Lee, P. S. Next-generation multifunctional electrochromic devices. *Acc. Chem. Res.* **49**, 1469–1476 (2016).

Publisher's note Springer Nature remains neutral with regard to jurisdictional claims in published maps and institutional affiliations.

© The Author(s), under exclusive licence to Springer Nature Limited 2020

Methods

Pulsed laser deposition of SrCoO_x thin films. BM-SCO thin films (~44 nm thick) were deposited onto YSZ substrates (10 mm × 5 mm × 0.5 mm; MTI Corp.) by using pulsed laser deposition. An ~10 nm thick gadolinia-doped ceria interlayer were deposited before the SCO deposition. A 248 nm KrF excimer laser was used for the pulsed laser deposition. The deposition temperature and p_{O_2} were 700 °C and 20 mtorr, respectively. The thin films were allowed to cool down to room temperature in the same p_{O_2} at a rate of 10 °C/min.

Ionic liquid and ion gel gating. Ionic liquid gating was done by using 1-hexyl-3-methylimidazolium bis(trifluoromethylsulfonyl)imide (HMIM-TFSI) as the gating electrolyte (Sigma-Aldrich). The ionic liquid was used as received. A Pt wire was spring loaded to be in contact either directly with the SrCoO_x thin-film surface (for oxidation) or with the silver-painted electrode (for hydrogenation, ~8 mm × 1 mm). The silver electrode was used for hydrogenation primarily to ensure enough electrical conductivity, as the formed H-SrCoO_x has a very low conductivity. The samples were immersed in ionic liquid with a wound Pt wire as the counter electrode. The counter electrode Pt wire was immersed into the ionic liquid so as to not touch the SCO thin film (Fig. 1b). A PARSTAT 4000 (Princeton Applied Research) potentiostat was used to apply biases between the sample and the Pt counter electrode. The gating experiments were performed in normal laboratory conditions without a deliberately controlled humidity. A USB camera was used to monitor the colour change of the thin-film samples during the phase transition. Typically, the oxidation (BM-SCO → P-SCO) reaction finished within 1 min, whereas hydrogenation (BM-SCO → H-SCO) required a much longer time to complete (~30 min).

Ion gels were fabricated following the methods reported by Lee et al.¹⁸. HMIM-TFSI and poly(vinylidene fluoride-co-hexafluoropropylene) were dissolved in acetone, and the resulting solution was solvent casted into gel films. The fabricated ion gels were cut and stuck to SCO thin films. Au foil was used as the electrode on top of the ion gels to apply a bias against the SCO samples. For both liquid- and gel-treated samples, the surface of the thin-film samples was cleaned using isopropanol and acetone thoroughly to remove any residue from ionic liquid or ion gel.

Electrical conductivity measurement. The electrical conductivity measurement was conducted using a Lake Shore 7504 Hall Effect/Cryogenic Hall Effect Electronic Transport Measurement System. Electronic resistivity was obtained using the current–voltage curves for the corresponding resistances of the van der Pauw configuration.

Soft XAS. Soft XAS measurements were performed at the IO-XAS endstation of the 23-ID-2 (IOS) beamline at National Synchrotron Light Source II. The XAS data were collected at room temperature in an ultrahigh vacuum condition (~10^{−9} torr) using the PFY mode. Residues of ionic liquid or ion gels were cleaned using isopropanol and acetone before loading samples into the ultrahigh vacuum chamber. Each measured PFY spectrum was normalized by the incident X-ray flux, which was measured by simultaneously recording the drain current from a highly transparent gold mesh upstream of the sample.

TDTR measurements. TDTR is described in detail in the literature^{19–21} and is briefly reviewed here. The Nanoengineering Group at the Massachusetts Institute of Technology uses a pulsed laser (Ti:sapphire) at 800 nm with a repetition rate of 80.7 MHz, pulse width of approximately 200 fs and power per pulse of 15 nJ from which the pump and probe beams are split using a polarizing beam-splitter. Prior to performing TDTR measurements, all the SCO thin-film samples were coated with an aluminium layer (80 nm nominal thickness) using electron-beam deposition. For the liquid- and gel-treated samples, the surface of the SCO was expunged of any remaining liquid or gel using isopropanol and acetone prior to the aluminium deposition. The laser beam comes from the top of the thin-film sample. Schmidt et al.²¹ describe more details of the TDTR measurements. We did find that the sample can relax even at ambient temperature over several days, especially after obtaining the P-SCO phase. Therefore, care was taken to minimize the time between sample fabrications and TDTR measurements (the fabrication, characterization and the measurement steps were performed within the same day). We believe that this approach can effectively ensure that the TDTR results are representative of the true states of different SCO phases. We also found that, after the aluminium metal layer deposition for TDTR measurements, the sample relaxation was significantly reduced. This capping layer serves to maintain the sample state by minimizing oxygen loss from the P-SCO film or hydrogen loss from the H-SCO film over time at ambient conditions. In fact, the temperature-dependent thermal conductivity data in Supplementary Fig. 13 were measured on the same samples prepared more than one year ago. As the changes in the sample's surface reflectance due to changes in temperature are small (~10^{−4} or less), a lock-in-amplifier detection scheme was used. The pump beam passes through an electro-optic modulator and is then converted into 400 nm using a bismuth borate crystal prior to striking the sample surface. The probe beam passes through the delay stage and then strikes the sample surface and the reflected probe is thus modulated at the same frequency as the pump. A photodiode coupled with an optical blue filter collects the probe signal, which is then passed to the

lock-in amplifier that is collecting at the selected modulation frequency. Owing to the interplay of sensitivity and noise (the details of which are discussed in the Supplementary Information), the data presented here were collected at modulation frequencies of 6 and 9 MHz.

The time traces obtained from TDTR were interpreted using a multilayer solution to the heat-diffusion equation²¹. Known material parameters (heat capacity and layer thickness) were passed as the input to the heat-transfer model, whereas the unknowns (the thermal conductivity of the film and the interface conductance between the aluminium layer and the film) were obtained through non-linear least squares minimization using the experimental data as the target set. The parameters used in the fitting procedure are reported in the Supplementary Information.

Ab initio calculations of thermal conductivity. We calculated the thermal conductivity of P-SCO by using density functional theory (DFT) with the temperature-dependent effective potential formalism^{35–37} and lattice dynamics. All the DFT and molecular dynamics based on DFT (DFT-MD) simulations were conducted with the Vienna ab initio simulation package (VASP 5.4.4)^{38–41}. First, the fully relaxed crystal structure of P-SCO was determined with DFT. Second, DFT-MD at 300 K was conducted. Third, forces and displacements of atoms collected from the DFT-MD simulations were recalculated with DFT of a higher accuracy and then fitted with ALAMODE⁴² to generate second- and third-order force constants. In strained P-SCO, the recalculation of forces and displacements was skipped with an acceptable error of around 6.6%. Finally, lattice dynamics simulations were performed to determine the phonon properties, and the Boltzmann transport equation with the relaxation time approximation was solved to obtain the thermal conductivities, using ALAMODE.

During the DFT and DFT-MD simulations, the generalized gradient approximation (GGA) with the Perdew–Burke–Ernzerhof exchange correlation functional⁴³ and a Hubbard U within the GGA + U approach⁴⁴ proposed by Dudarev et al.⁴⁵ was used. For the Co d electrons, the on-site Coulomb interaction U and exchange interaction J were chosen to be 2.5 eV and 1.0 eV, respectively, according to the previous report⁴⁶. Pseudo-potentials created from the projector augmented wave method^{38,47} were used. The plane-wave energy cutoff was set to 700 eV. P-SCO was modelled with a 135 atom supercell. Strained P-SCO had the same supercell as unstrained P-SCO, with isotropically compressed or stretched lattice constants. The Monkhorst–Pack k -point meshes were 3 × 3 × 3 for DFT-MD, and 5 × 5 × 5 for DFT. Structural relaxations were conducted until all the forces were smaller than 0.0001 eV Å^{−1}. The exchange correlation functionals were corrected with the Vosko–Wilk–Nusair interpolation⁴⁸. The ferromagnetic structure was assumed in P-SCO. We note that P-SCO at 300 K is paramagnetic¹²; however, simultaneously sampling magnetic configurations and crystal structures in the paramagnetic state near the magnetic transition temperature is unfeasible. DFT-MD used the Nosé thermostat^{49,50} to maintain the temperature of 300 K. The time step in DFT-MD was 2 fs. Thermal conductivities were calculated on q -point meshes with different sizes and extrapolated to the q -point mesh with infinite size by using the reported formula⁵¹, $\frac{\kappa_n(T)}{\kappa_0(T)} = 1 - \frac{c(T)}{n}$, where $\kappa_n(T)$ and $\kappa_0(T)$ are thermal conductivities at temperature T on the meshes with $n \times n \times n$ q points and with an infinite number of q points, respectively, and $c(T)$ is a constant at temperature T .

Data availability

Experimental and computational data are available from the corresponding authors on reasonable request.

References

- Hellman, O., Abrikosov, I. A. & Simak, S. I. Lattice dynamics of anharmonic solids from first principles. *Phys. Rev. B* **84**, 180301 (2011).
- Hellman, O., Steneteg, P., Abrikosov, I. A. & Simak, S. I. Temperature dependent effective potential method for accurate free energy calculations of solids. *Phys. Rev. B* **87**, 104111 (2013).
- Hellman, O. & Abrikosov, I. A. Temperature-dependent effective third-order interatomic force constants from first principles. *Phys. Rev. B* **88**, 144301 (2013).
- Kresse, G. & Joubert, D. From ultrasoft pseudopotentials to the projector augmented-wave method. *Phys. Rev. B* **59**, 1758–1775 (1999).
- Kresse, G. & Furthmüller, J. Efficient iterative schemes for ab initio total-energy calculations using a plane-wave basis set. *Phys. Rev. B* **54**, 11169–11186 (1996).
- Kresse, G. & Hafner, J. Ab initio molecular dynamics for open-shell transition metals. *Phys. Rev. B* **48**, 13115–13118 (1993).
- Kresse, G. & Furthmüller, J. Efficiency of ab-initio total energy calculations for metals and semiconductors using a plane-wave basis set. *Comput. Mater. Sci.* **6**, 15–50 (1996).
- Tadano, T., Gohda, Y. & Tsuneyuki, S. Anharmonic force constants extracted from first-principles molecular dynamics: applications to heat transfer simulations. *J. Phys. Condens. Matter* **26**, 225402 (2014).
- Perdew, J. P., Burke, K. & Ernzerhof, M. Generalized gradient approximation made simple. *Phys. Rev. Lett.* **77**, 3865–3868 (1996).

44. Anisimov, V. I., Zaanen, J. & Andersen, O. K. Band theory and Mott insulators: Hubbard U instead of Stoner I . *Phys. Rev. B* **44**, 943–954 (1991).
45. Dudarev, S. L., Savrasov, S. Y., Humphreys, C. J. & Sutton, A. P. Electron-energy-loss spectra and the structural stability of nickel oxide: An LSDA+ U study. *Phys. Rev. B* **57**, 1505–1509 (1998).
46. Lee, J. H. & Rabe, K. M. Coupled magnetic-ferroelectric metal-insulator transition in epitaxially strained SrCoO_3 from first principles. *Phys. Rev. Lett.* **107**, 067601 (2011).
47. Blochl, P. E. Projector augmented-wave method. *Phys. Rev. B* **50**, 17953–17979 (1994).
48. Vosko, S. H., Wilk, L. & Nusair, M. Accurate spin-dependent electron liquid correlation energies for local spin density calculations: a critical analysis. *Can. J. Phys.* **58**, 1200–1211 (1980).
49. Nosé, S. A unified formulation of the constant temperature molecular dynamics methods. *J. Chem. Phys.* **81**, 511–519 (1984).
50. Nosé, S. Constant temperature molecular dynamics methods. *Prog. Theor. Phys. Suppl.* **103**, 1–46 (1991).
51. Shiomi, J., Esfarjani, K. & Chen, G. Thermal conductivity of half-Heusler compounds from first-principles calculations. *Phys. Rev. B* **84**, 104302 (2011).

Acknowledgements

This work was supported primarily by the MRSEC Program of the National Science Foundation under award number DMR-1419807. This work made use of the Shared Experimental Facilities supported in part by the MRSEC Program of the National Science Foundation under award number DMR-1419807. This research used the IOS Beamline of the National Synchrotron Light Source II, a US Department of Energy (DOE) Office of Science User Facility operated for the DOE Office of Science by Brookhaven National Laboratory under contract no. DE-SC0012704. We thank P. Yu from Tsinghua University and his co-workers for sharing the crystal structure files of H-SCO used for the

visualization in Fig. 1a. The authors acknowledge the support of computational resources from the National Energy Research Scientific Computing Center (NERSC), a US DOE Office of Science User Facility operated under contract no. DE-AC02-05CH11231; the MIT-PSFC partition of the Engaging cluster at the MGHPCC facility, which was funded by DOE grant no. DE-FG02-91-ER54109, and the MIT-NSE partition funded by MIT; the Extreme Science and Engineering Discovery Environment (XSEDE) Stampede2 at Texas Advanced Computing Center through allocation TG-DMR120025, which is supported by National Science Foundation grant no. ACI-1548562. Q.S. thanks B. Song, K. Chen and J. Zhou for help with TDTR measurements. H.Z. thanks O. Hellman, T. Tadano, J. Yang, L. Sun and Y. Chi for technical help and fruitful discussions.

Author contributions

Q.L. and J.W. prepared the SCO thin-film samples and performed the electrochemical gating of SCO films by using YSZ, ionic liquid and ion gel as the electrolytes. S.H. and Q.S. performed the TDTR measurements, and H.Z. did the first-principles simulations. Q.L., G.V., I.W. and A.H. performed the XAS measurements. All the authors discussed the results and contributed to the writing of the manuscript. B.Y. and G.C. originated and supervised the research.

Competing interests

The authors declare no competing interests.

Additional information

Supplementary information is available for this paper at <https://doi.org/10.1038/s41563-020-0612-0>.

Correspondence and requests for materials should be addressed to G.C. or B.Y.

Reprints and permissions information is available at www.nature.com/reprints.